Key Points:
- A multistage rupture process of the 2015 Nepal earthquake is observed
- Stage 1 of the 2015 Nepal earthquake is weak and slow
- Stage 2 of the 2015 Nepal earthquake is high-frequency deficient

Supporting Information:
- Figure S1
- Figure S2
- Figure S3
- Figure S4
- Figure S5
- Figure S6
- Figure S7
- Figure S8
- Figure S9
- Figure S10
- Text S1

Correspondence to:
W. Fan,
w3fan@ucsd.edu

Detailed rupture imaging of the 25 April 2015 Nepal earthquake using teleseismic *P* waves

Wenyuan Fan[1] and Peter M. Shearer[1]

[1]Scripps Institution of Oceanography, University of California, San Diego, La Jolla, California, USA

Abstract We analyze the rupture process of the 25 April 2015 Nepal earthquake with globally recorded teleseismic *P* waves. The rupture propagated east-southeast from the hypocenter for about 160 km with a duration of ~55 s. Backprojection of both high-frequency (HF, 0.2 to 3 Hz) and low-frequency (LF, 0.05 to 0.2 Hz) *P* waves suggest a multistage rupture process. From the low-frequency images, we resolve an initial slow downdip (northward) rupture near the nucleation area for the first 20 s (Stage 1), followed by two faster updip ruptures (20 to 40 s for Stage 2 and 40 to 55 s for Stage 3), which released most of the radiated energy northeast of Kathmandu. The centroid rupture power from LF backprojection agrees well with the Global Centroid Moment Tensor solution. The spatial resolution of the backprojection images is validated by applying similar analysis to nearby aftershocks. The overall rupture pattern agrees well with the aftershock distribution. A multiple-asperity model could explain the observed multistage rupture and aftershock distribution.

1. Introduction

A M_w 7.8 earthquake struck central Nepal on 25 April 2015 with an epicenter 77 km northwest of Kathmandu. With over 8000 fatalities, it is the largest and most destructive earthquake since the 1934 Bihar-Nepal earthquake in this region [*Singh and Gupta*, 1980; *Bilham*, 2004]. The Global Centroid Moment Tensor (GCMT) [*Ekström et al.*, 2012] favors a nodal plane with strike 293°, dip 7° to the north, and rake 108°, and the preliminary finite-fault model from the U.S. Geological Survey National Earthquake Information Center (NEIC) shares a similar solution (strike 295° and dip 10°). The hypocenter depth is 15 km, indicating the quake occurred on the Main Himalayan Thrust fault (MHT). This fault has been known to host reoccurring large events [e.g., *Ambraseys and Douglas*, 2004; *Bilham*, 2004]. The GPS-derived convergence rate between India and South Tibet ranges from 17.8 ± 0.5 mm/yr to 20.5 ± 1 mm/yr from central and eastern Nepal to western Nepal [*Ader et al.*, 2012]. Because of the large moment deficit accumulation on the MHT within Nepal, it has been suggested that the fault would be able to host a M_w 9.2 earthquake with a return period of the order of 3000 years, if all the moment is released seismically [*Ader et al.*, 2012].

For large earthquakes, the teleseismic *P* wave train contains details of the spatiotemporal slip distribution and rupture propagation. This is illustrated for the Nepal earthquake in Figure 1, which shows that the displacement envelope functions of the low-frequency *P* waves exhibit a clear azimuthal pattern from 40 s to 65 s, with an average duration of 55 s. Assuming that the *P* wave signals are mostly from the rupture front, then the rupture direction is about 130°. Following *Ni et al.* [2005], we can estimate that the rupture length is about 160 km with an average rupture speed of ~2.9 km/s (see supporting information). This rupture length agrees well with the aftershock distribution. To resolve details during the rupture propagation, we plot the seismograms versus the directivity parameter defined in *Ammon et al.* [2005] and *Zhan et al.* [2014] (see supporting information), assuming a rupture direction of 130°. As shown in Figure 1, this plot reveals three distinct subevents, with times and epicentral distances that can be directly estimated from the intercepts and slopes of lines connecting the subevent pulses on each seismogram. These events occurred at times of 24 s, 36 s, and 47 s, and distances of 54 km, 85 km, and 115 km, with respect to the hypocenter.

Although this approach is useful for providing a quick view of some of the main details of the rupture, it has limited resolution because the records outside of the three largest subevents are too weak to distinguish finer details and the method assumes that the rupture propagates in a one-dimensional fashion only, and thus, we cannot image possible two-dimensional variations in radiation within the rupture plane. To learn more, we apply *P* wave backprojection to image more directly the rupture properties of the Nepal earthquake.
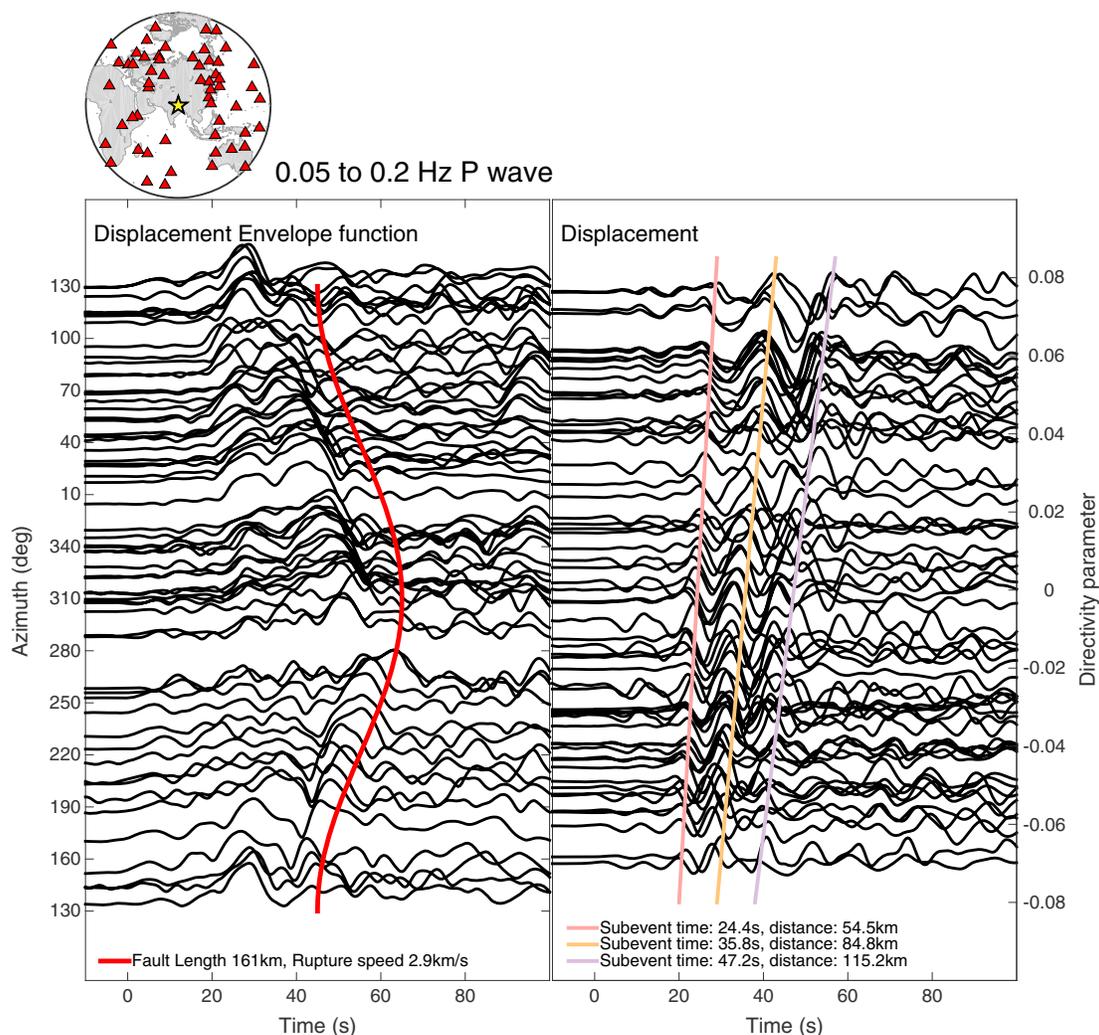
Figure 1. (top) Station map. (bottom left) Low-frequency *P* wave displacement envelope functions plotted versus azimuth. The envelope functions are calculated using the Hilbert transform and are smoothed with a moving average window of 2.5 s half-width. The red line shows the expected rupture duration for a fault length of 160 km and an average rupture velocity of 2.9 km/s. (bottom right) *P* wave displacements versus directivity parameter [*Ammon et al.*, 2005], assuming 130° as the rupture direction. The onset of the *P* wave begins at 0 s. Three different subevents are indicated with the colored lines.

Since its introduction by *Ishii et al.* [2005] for the 2004 Sumatra earthquake, the backprojection method has been widely applied to large earthquake imaging, most often using regional arrays such as Hi-net or USArray [e.g., *Meng et al.*, 2011; *Wang et al.*, 2012; *Meng et al.*, 2012; *Koper et al.*, 2011; *Kiser and Ishii*, 2012]. However, in principle, higher resolution can be obtained using globally distributed stations [e.g., *Walker et al.*, 2005; *Yagi et al.*, 2012; *Okuwaki et al.*, 2014] and this is the approach we adopt here. We analyze both a high-frequency band (0.2 to 3 Hz), similar to that used most often in prior backprojection studies, and a low-frequency band (0.05 to 0.2 Hz) to provide a more complete description of the seismic radiation.

Our results indicate that the rupture has three stages, with the first stage rupturing eastward in the downdip direction and the later two stages involving eastward rupture in the updip direction. The second rupture stage radiated most of the energy within the bandwidth of our study, and its location and time agree well with the GCMT solution and preliminary finite-fault models from the NEIC and Geospatial Information Authority of Japan (GSI) (www.gsi.go.jp). Integrating our results with the aftershock distribution, current available finite-fault models, and centroid moment solutions, we propose a multiple-asperity model. Finally, we compare our results with source models of the 2005 Kashmir earthquake to explore common characteristics and differences among continental earthquakes in the Himalayan region.
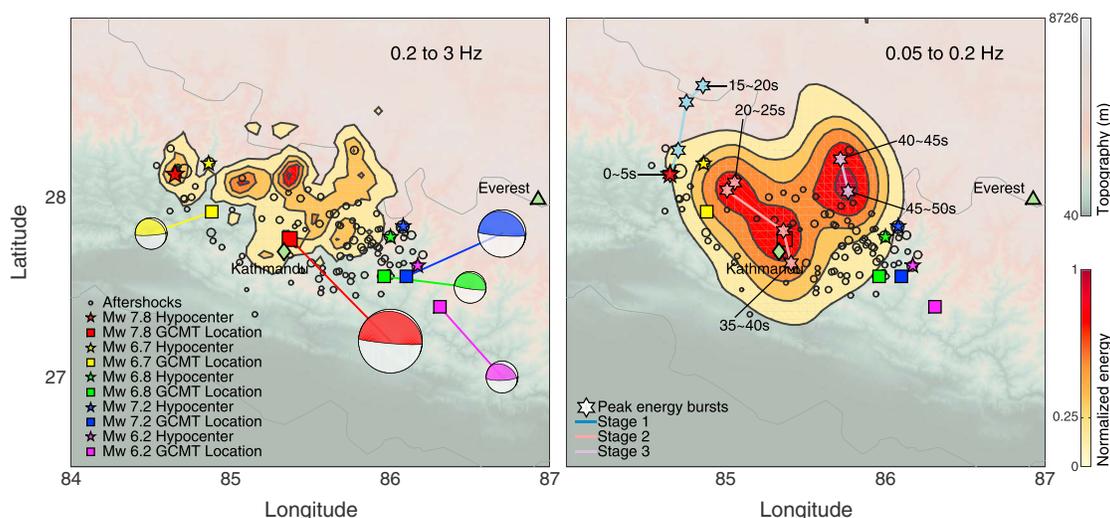
Figure 2. Time-integrated images of backprojected *P* waves. (left) High-frequency (HF) backprojection image over 60 s with maximum power normalized to 1. (right) Low-frequency (LF) backprojection image over 60 s with maximum power normalized to 1. Background topography is obtained from topex.ucsd.edu [*Smith and Sandwell*, 1997].

2. Method and Data

The backprojection method assumes that the initial *P* wave arrival comes from the hypocenter, but later parts of the *P* wave train likely contain overlapping contributions from different parts of the ensuing rupture. We follow the method described in *Ishii et al*. [2005] and *Walker et al*. [2005], with *N*th root stacking *Xu et al*. [2009] to suppress noise. A 1-D velocity model (IASP91 [*Kennett and Engdahl*, 1991]) is used to predict theoretical *P* wave traveltimes. We empirically correct the traveltime deviations that are due to 3-D velocity structure by aligning the initial *P* arrival [*Reif et al.*, 2002]. The aligned far-field seismograms are then backprojected to a grid of possible sources around the hypocenter to constructively interfere if they are true source locations, or to destructively interfere if they are not. For a given grid point, the start time of coherent energy bursts represents the onset time of the rupture at that position, and the integrated power indicates the relative intensity of *P* wave radiation at that point. The source depth is poorly constrained by far-field *P* waves; therefore, the source depths are fixed to the hypocentral depth and the potential source locations are functions only of latitude and longitude. Nonlinear stacking approaches like *N*th root stacking were originally designed to reduce false alarms in seismic array detection [*Rost and Thomas*, 2002]. They can effectively suppress noise and enhance the coherent signals when applied to backprojection [*Xu et al.*, 2009], at the cost of losing absolute amplitude information. Detailed discussion about the effects of *N* can be found in *McFadden et al*. [1986]; in this study, we use $N = 4$ as suggested in *Xu et al*. [2009].

The investigated area is 400 km by 400 km with a 5 km grid point spacing, within the latitude range 26.34° to 29.92° and longitude range 83.63° to 87.70°. We use seismograms from stations of the broadband Global Seismic Network distributed by the Data Management Center (DMC) of Incorporated Research Institutions for Seismology (IRIS) (Figure 1). We select 62 stations with high signal-to-noise ratios with epicentral distances ranging from 30° to 90°, thus avoiding the waveform complexities at shorter ranges from the upper mantle discontinuities and at longer ranges from the lowermost mantle near the core-mantle boundary. The azimuth ranges from 3.9° to 347.7° (Figure 1); the good azimuthal coverage greatly reduces backprojection artifacts and enables a relatively high spatial resolution. With a 40 Hz sample rate, the seismic data are filtered into three frequency bands (0.05–0.2 Hz (low frequency, LF), 0.1–1 Hz (middle frequency, MF), and 0.2–3 Hz (high frequency, HF)) to investigate potential frequency-dependent behavior. All three frequency bands use the same alignment obtained from the cross correlation of MF band data (Figure S1 in the supporting information). To save space, only the LF and HF results are described in the main paper; as might be expected, the MF results generally lie between these two end-member frequency bands (see supporting information).

The amplitude of the *P* wave train is normalized to neutralize the variations caused by site effects, the radiation pattern, and different instrument gains. To avoid biased backprojection results from noisy and/or
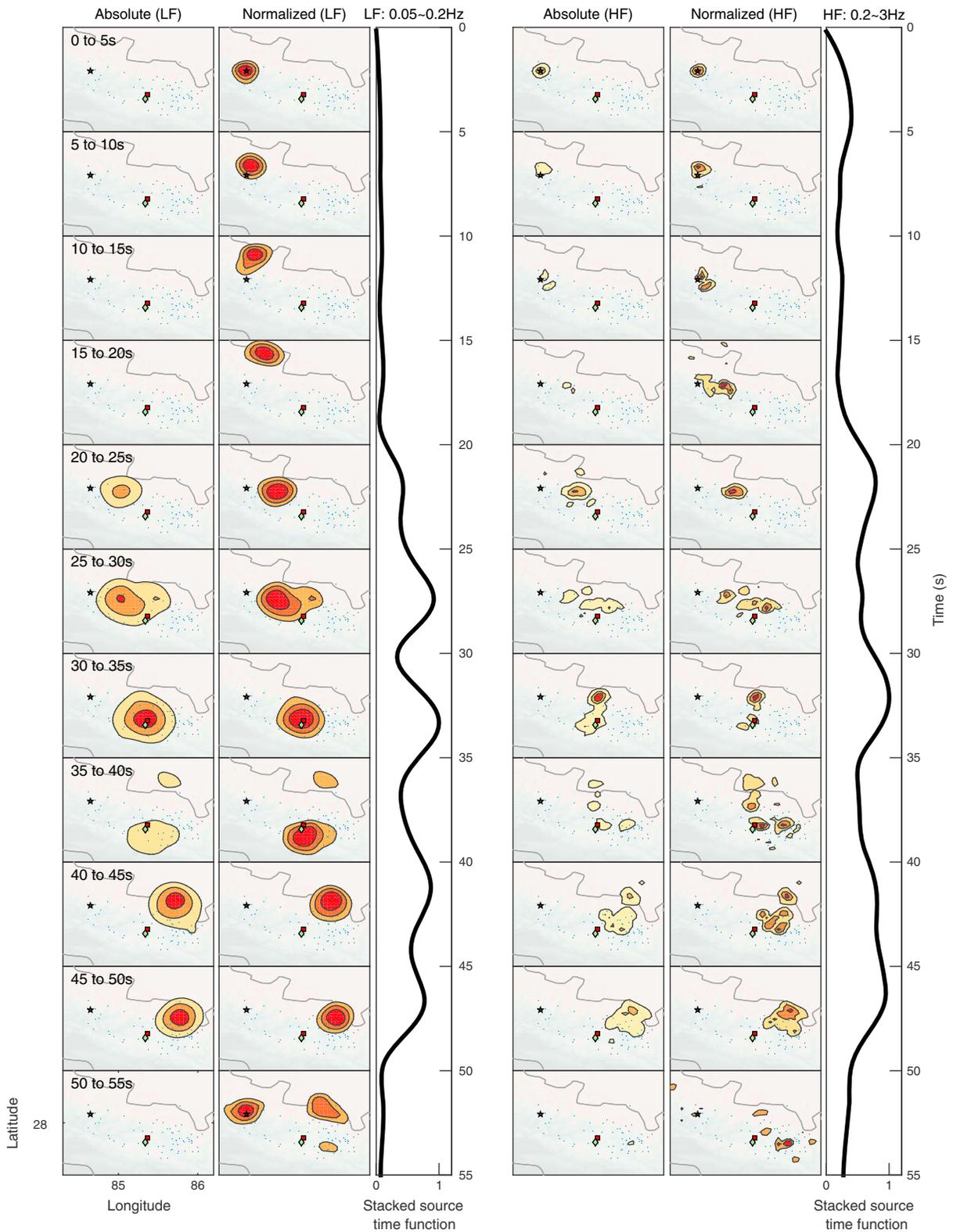
Figure 3. Snapshots of both low-frequency (LF) and high-frequency (HF) backprojections compared with the stacked source time functions.
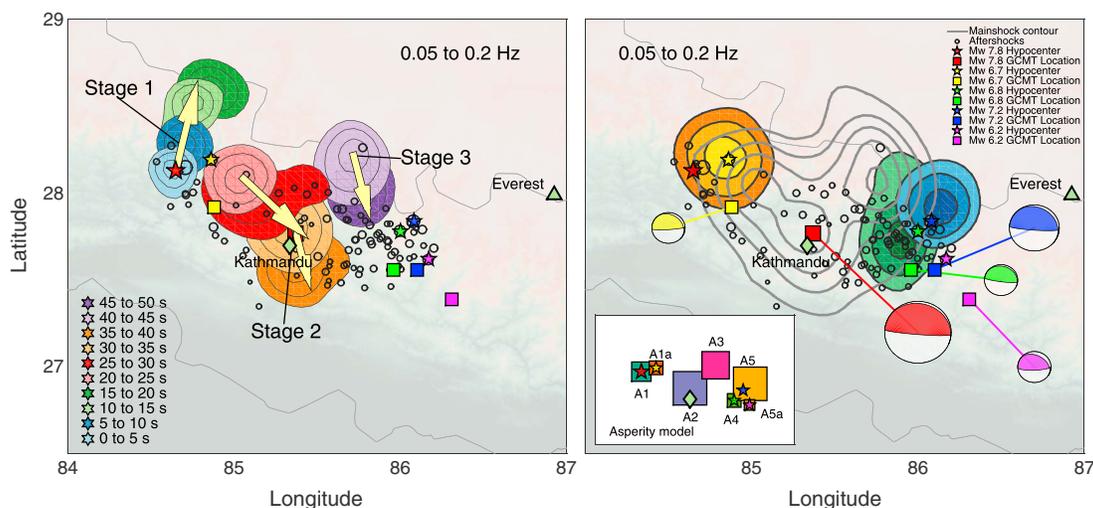
Figure 4. (left) Rupture evolution of the M_w 7.8 main shock imaged with low-frequency (LF) backprojection. The different inferred rupture stages are shown as the yellow arrows, labeled 1 to 3. (right) LF backprojection images of M_w 6.7, M 6.8, and M_w 7.2 aftershocks overlaid with the main shock rupture contour. The integrated energy for three aftershocks is differentiated with different colors: yellow for M_w 6.7, green for M_w 6.8, and blue for M_w 7.2. Inset: a possible asperity model.

overrepresented regions, stations are weighted by their average correlation coefficients from the alignment and inversely with the number of contributing stations within 5°. No postsmoothing or postprocessing is applied to the images.

3. Results

The integrated backprojected energy over the ~60 s duration of the rupture is shown in Figure 2. Both HF and LF backprojection show the rupture zone is mostly east and southeast of the epicenter with a rupture length about 165 km (1.5° in longitude); and both HF and LF backprojection show major energy release north of Kathmandu (Figure 2). A M_w 6.7 aftershock occurred half an hour after the main shock close to the hypocenter; a M_w 6.8 aftershock occurred 1 day later at the eastern boundary of the main shock rupture. On 12 May 2015, a M_w 7.2 aftershock occurred 83 km northeast of Kathmandu, which is close to the M_w 6.8 aftershock, and half an hour later, a M_w 6.2 earthquake occurred close to the M_w 7.2 aftershock. Most of the HF energy was released north of Kathmandu, while the LF energy bursts show another energy release peak beneath Kathmandu (Figure 2). Locations of the peak energy bursts seen in the LF backprojection with 5 s windows are labeled in Figure 2, illuminating a multistage rupture process. In the LF-integrated energy image, the centroid rupture power agrees well with the GCMT solution (Figure 2).

Snapshots of both the HF and LF radiation distribution show the rupture propagation details (Figure 3). From the absolute LF-integrated power images (normalized with the maximum power over the entire 60 s) and stacked LF source time functions, weak rupture propagation during the first 20 s can be observed. The normalized LF-integrated power images (normalized with the maximum power of each 5 s window) reveal an initial northeast downdip rupture (Stage 1). From 20 to 40 s, the LF-integrated energy climbed to its maximum and a southeast updip rupture propagated toward Kathmandu (Stage 2). From 30 to 35 s, the LF-integrated power concentrated around the GCMT centroid location, which is next to Kathmandu. From 40 to 50 s, another southeast updip rupture broke the northeastern part of the fault and propagated parallel to the 20 to 40 s rupture (Stage 3). These three rupture stages are labeled with hexagrams in Figure 2 and labeled with yellow arrows in Figure 4 (left). Compared to the LF images, relatively more HF energy was released during the initiation stage (Figures 2–4). From 10 to 25 s, the HF image shows eastward rupture propagation heading into where the Stage 3 rupture starts. The HF energy release reached its maximum from 30 to 35 s west of the Stage 3 rupture and ~50 km north of Kathmandu. The HF snapshot at 35 to 40 s suggests a rupture around the Stage 3 rupture, and from 40 to 50 s, the HF images are similar to the LF images. From 50 to 55 s, the normalized LF image indicates new rupture near the hypocenter area. However, bootstrap resampling tests (see next section) suggest that this is not a robust feature, so we cannot be confident that it is not some kind of backprojection artifact in the absence of other supporting observations.

4. Discussion

The rupture velocity varies among the three stages. The earthquake had a slow start; assuming the Stage 1 rupture followed the path indicated in Figure 2, the average rupture velocity is ~2 km/s. In Stage 2, the distance between the peak energy bursts of 25–30 s and 30–35 s is ~46 km. If the rupture propagated linearly, the apparent rupture velocity is 4.6 km/s, which is faster than the local S wave velocity [*Laske et al.*, 2013]. The rupture velocity during Stage 3 would be ~2 km/s if it followed the direct path shown in Figure 2. However, we cannot constrain the rupture behavior outside of the times of large radiation bursts. For example, instead of traveling directly from the hypocenter (or other reference point) through an asperity, the rupture could proceed around the asperity before causing it to break from the side and rupture at a misleadingly high apparent velocity away from the hypocenter. In this case the apparent rupture velocity at times could be much higher than the true rupture velocity. By projecting the backprojected energy to certain azimuths, all three stages can display very fast rupture speeds (Figure S4). To better constrain the possible rupture velocities, near-field seismic observations will be needed.

To understand the uncertainties and robustness of the backprojection images, we have performed three types of resolution tests. First, the theoretical resolution can be evaluated by randomly assigning a single recorded P wave train to all the stations, then performing backprojection with these traces. This provides a measure of the likely resolution of the station distribution given the frequency content of the data. As seen in Figure S5, as expected the spatial resolution is proportional to the bandwidth used for backprojection, and the theoretical spatial resolution of the LF data is about 50 km in radius.

Another way to test the resolution is to perform backprojection on aftershocks with similar station coverage as the main shock. In this way, the complexities of the wavefield are taken into account, and due to the fact that the aftershocks have fewer usable stations and may themselves have finite rupture areas, the resolution during the main shock should be at least as good as that seen in the aftershock images. We performed back-projection on the M_w 6.7, M_w 6.8, and M_w 7.2 aftershocks using 53, 56, and 56 records, respectively. We did not attempt to backproject the 12 May 2015 M_w 6.2 aftershock because of its relatively poor P wave signal-to-noise ratio. The integrated energies of these three aftershocks are shown in Figures 4, S6, and S7. The M_w 6.7 event occurred half an hour after the main shock, so the P wave train is severely contaminated by the main shock surface wave, which leads to lower spatial resolution compared to the M_w 6.8 aftershock (Figure S6). Snapshots and stacked source time functions (see Figure S8) for the M_w 7.2 aftershock indicate a complicated rupture lasting about 20 s, with at least two subevents. The time-integrated LP image for the M_w 7.2 event does not appear larger than the M_w 6.8 rupture image, suggesting that the M_w 7.2 rupture may have been relatively compact and likely of higher stress drop than the M_w 6.8 event (Figure S7).

From Figure 4, the spatial extent of the Stage 2 and the Stage 3 ruptures imaged in the main shock is comparable to the spatial extent of the aftershocks, showing that the distinct subevents are clearly resolved. As a final test, we performed bootstrap resampling to verify the stability of our results with respect to random variations in the stations sampling the main shock. With the exception of the LP results at 50 to 55 s (see above), we found that all of the main features imaged in the backprojection results are robust; i.e., they appear in over 95% of the bootstrap resampled images. Details of the bootstrap analysis are presented in the supporting information.

Artifacts in backprojection images may arise due to complicated waveforms, depth phases, or limited station coverage, which may contribute to misleading or erroneous interpretations of the rupture process. The good azimuthal coverage of the teleseismic data minimizes the "swimming" artifacts [e.g., *Xu et al.*, 2009; *Koper et al.*, 2012] that are troublesome in backprojection images from regional arrays. For large shallow earthquakes, depth phases will be present that cannot easily be separated from the direct phases. Because depth phases occur close in time and at similar slowness to the direct phases, they will backproject to locations near the direct phase image at only slightly later times, and thus, depth-phase effects are often ignored in backprojection studies of large earthquakes. However, for the high-resolution imaging at 5 s intervals that we perform here it is important to examine the possible biasing effects of depth phases as well as interference effects from multiple sources. We tested the observed multistage rupture propagation with a multiple point source synthetic test (which includes depth phases computed from the GCMT solution) and a depth-phase deconvolution analysis and found that depth phases and other complexities do not bias our results very much (Figure S9 and S10). All of the main features that we image are robust, although the depth phases extend the duration of the radiation at some source locations by about 5 s.

The earthquake rupture propagation is primarily unilateral with possible multiple branches (Figures 2–4). Combining both LF and HF images, one possible scenario is that the rupture front reached Stage 2 and Stage 3 around the same time after the initiation; but the part of the fault resolved as Stage 3 did not break until the observed Stage 2 rupture passed Kathmandu. The Stage 2 rupture imaged at LF is less obvious in HF results. This suggests that the Stage 2 rupture revealed by the LF images is deficient in high-frequency energy. The cause of this HF deficit is unclear, which will need further investigation. The HF peak energy burst locates at the edge of the Stage 3 rupture and does not colocate with the centroid location. On the other hand, the LF backprojection results agree well with the centroid moment tensor solution both temporally and spatially (Figure 2). The aftershocks of the Nepal earthquake are distributed compactly within the backprojection imaged region (Figure 2 and 4), with the M_w 6.7 aftershock near the west edge of the mains hock, and the M_w 6.8 and M_w 7.2 aftershocks on the eastern side. Noticeably, the epicentral distance between the M_w 6.8 and M_w 7.2 aftershocks is within 10 km. In addition, the majority of the aftershocks concentrate at the eastern edge of the main shock.

One plausible explanation for the observed rupture pattern and the aftershock seismicity is a multiple-asperity model as illustrated in Figure 4: the main shock is dominated by three asperities, indicated as A1, A2, and A3, which correspond to the three rupture stages. The M_w 6.7 aftershock is labeled as A1a in Figure 4 and may be an unbroken remnant of A1 from the main shock rupture. The M_w 6.8 aftershock is labeled as A4 and ruptured 1 day later at the east boundary of the main shock. The M_w 7.2 aftershock is labeled as A5 and occurred 2 weeks later, followed by a M_w 6.2 aftershock denoted as A5a. Because of the spatial clustering of the M_w 6.8, M_w 7.2, and M_w 6.2 events, it is possible that A4, A5, and A5a are three parts of one large asperity that ruptured sequentially. However, because we can resolve only the main sources of seismic radiation, we cannot image the connecting segments that might verify this; thus, the three stages of the main shock are not necessarily directly spatially connected or temporally linked into a sequence.

The GSI quickly released crustal deformation observations obtained with synthetic aperture radar. The interferometric analysis shows a major displacement (≥10 cm) area extending about 160 km in the east-west direction, which agrees well with our directivity analysis (section 3). The preliminary finite-fault model released by GSI has maximum slip (>4 m) beneath the area 20 to 30 km northeast of Kathmandu, which is consistent with the observed Stage 2 rupture. In the GSI slip model, there is a significant slip patch north of the hypocenter, which validates the Stage 1 rupture observed in our LF backprojection. The ScanSAR (synthetic aperture radar (SAR) with a swath coverage) of Advanced Land Observing Satellite 2 (ALOS-2) show two patches of line-of-sight deformation outside of the 500 mm deformation contour (E. Lindsey et al., Line of sight deformation from ALOS-2 interferometry: M_w 7.8 Gorkha earthquake and M_w 7.3 aftershock, submitted to *Geophysical Research Letters*, 2015) that are possibly due to the Stage 3 rupture and the aftershocks (Figure 4).

The faults defining the India and Eurasia plate boundary have been repeatedly active due to the continental collision. There were four great earthquakes with magnitudes ∼ M_w 8 along the boundary between 1897 to 1950 [*Bilham*, 2004]. Similar to the 2015 Nepal earthquake, none of the four events ruptured to the surface [*Bilham*, 2004]. The most recent large earthquake occurring on this boundary was the 2005 Kashmir earthquake. Both events appear to be simple shallow crustal events with compact slip distributions and both apparently nucleated at the edge of their main asperities [*Avouac et al.*, 2006]. The 2005 Kashmir earthquake initiated at the bottom edge of the main slip patch, and the 2015 Nepal earthquake nucleated at the western edge of its rupture zone. Both earthquakes apparently ruptured more than one asperity [*Parsons et al.*, 2006; *Pathier et al.*, 2006]. Although the 2005 Kashmir earthquake was smaller than the 2015 Nepal earthquake, it was more destructive, which led to over 80,000 casualties. Besides the difference of population densities (194 km^2 for Nepal and 236 km^2 for Pakistan, according to the World Bank), possible explanations lie within the rupture differences: for the 2005 Kashmir earthquake, the dip angle was ∼30°, which caused a very steep thrust-faulting event; the rupture was bilateral and propagated to the surface, which excited more surface waves; the major slip was constrained to be shallower than 10 km; and the short rise time (2–5 s) led to severe ground shaking [*Avouac et al.*, 2006; *Parsons et al.*, 2006; *Pathier et al.*, 2006]. In contrast, the 2015 Nepal earthquake did not rupture to the surface with unilateral propagation; with a 10° dip, the rupture was concentrated in the depth range of 8 to 20 km and the observed Stage 2 is high-frequency deficient, which could be a major reason why there was less ground motion (Figure 2).

5. Conclusion

Teleseismic P waves for the 2015 Nepal earthquake indicate that the rupture propagated for ∼160 km at an azimuth of ∼130° and an average rupture velocity of 2.9 km/s. We apply a global seismic network backprojection method to both low-frequency (LF, 0.05 to 0.2 Hz) and high-frequency (HF, 0.2 to 3 Hz) data, which provides good spatial resolution. The LF backprojection images suggest a three-stage rupture process: first, downdip rupture at the nucleation area for the first 20 s, then updip rupture which released most of the radiated energy from 20 to 40 s, and a terminating stage with updip rupture northeast of Kathmandu. The total rupture lasted for ∼55 s. We observe a relatively compact rupture pattern that agrees well with the aftershock distribution. A multiple-asperity model can explain the observed multistage rupture and the aftershock distribution. The apparent rupture velocity is significantly higher than S wave speed during the Stage 2 rupture, but we cannot be sure that this represents the true rupture speed. Given the current plate convergence rate, the M_w 7.8 earthquake is smaller than expected [*Ader et al.*, 2012]. Therefore, detailed imaging of the rupture process is important for future hazard assessments.

References

Ader, T., et al. (2012), Convergence rate across the Nepal Himalaya and interseismic coupling on the Main Himalayan Thrust: Implications for seismic hazard, *J. Geophys. Res.*, *117*, B04403, doi:10.1029/2011JB009071.

Ambraseys, N. N., and J. Douglas (2004), Magnitude calibration of north Indian earthquakes, *Geophys. J. Int.*, *159*(1), 165–206, doi:10.1111/j.1365-246X.2004.02323.x.

Ammon, C. J., et al. (2005), Rupture process of the 2004 Sumatra-Andaman earthquake, *Science*, *308*(5725), 1133–1139, doi:10.1126/science.1112260.

Avouac, J.-P., F. Ayoub, S. Leprince, O. Konca, and D. V. Helmberger (2006), The 2005, M_w 7.6 Kashmir earthquake: Sub-pixel correlation of ASTER images and seismic waveforms analysis, *Earth Planet. Sci. Lett.*, *249*(3–4), 514–528, doi:10.1016/j.epsl.2006.06.025.

Bilham, R. (2004), Earthquakes in India and the Himalaya: Tectonics, geodesy and history, *Ann. Geophys.*, *47*(2–3), 839–858.

Ekström, G., M. Nettles, and A. Dziewoński (2012), The global CMT project 2004–2010: Centroid-moment tensors for 13,017 earthquakes, *Phys. Earth Planet. Inter.*, *200–201*, 1–9, doi:10.1016/j.pepi.2012.04.002.

Ishii, M., P. M. Shearer, H. Houston, and J. E. Vidale (2005), Extent, duration and speed of the 2004 Sumatra–Andaman earthquake imaged by the Hi-net array, *Nature*, *435*(7044), 933–936.

Kennett, B. L. N., and E. R. Engdahl (1991), Traveltimes for global earthquake location and phase identification, *Geophys. J. Int.*, *105*(2), 429–465, doi:10.1111/j.1365-246X.1991.tb06724.x.

Kiser, E., and M. Ishii (2012), Combining seismic arrays to image the high-frequency characteristics of large earthquakes, *Geophys. J. Int.*, *188*(3), 1117–1128, doi:10.1111/j.1365-246X.2011.05299.x.

Koper, K. D., A. H. T. Lay, C. Ammon, and H. Kanamori (2011), Frequency-dependent rupture process of the 2011 M_w 9.0 Tohoku earthquake: Comparison of short-period P wave backprojection images and broadband seismic rupture models, *Earth Planets Space*, *63*(7), 599–602.

Koper, K. D., A. R. Hutko, T. Lay, and O. Sufri (2012), Imaging short-period seismic radiation from the 27 February 2010 Chile (M_w 8.8) earthquake by back-projection of P, PP, and PKIKP waves, *J. Geophys. Res.*, *117*, B02308, doi:10.1029/2011JB008576.

Laske, G., G. Masters, Z. Ma, and M. Pasyanos (2013), Update on CRUST1.0-A 1-degree global model of Earth's crust. Geophys. Res. Abstracts Vol. 15, EGU2013-2658 presented at EGU General Assembly 2013, held 7–12 April, 2013 in Vienna, Austria.

McFadden, P. L., B. J. Drummond, and S. Kravis (1986), The Nth–root stack: Theory, applications, and examples, *Geophysics*, *51*(10), 1879–1892, doi:10.1190/1.1442045.

Meng, L., A. Inbal, and J.-P. Ampuero (2011), A window into the complexity of the dynamic rupture of the 2011 M_w 9 Tohoku-Oki earthquake, *Geophys. Res. Lett.*, *38*, L00G07, doi:10.1029/2011GL048118.

Meng, L., J.-P. Ampuero, J. Stock, Z. Duputel, Y. Luo, and V. C. Tsai (2012), Earthquake in a maze: Compressional rupture branching during the 2012 M_w 8.6 Sumatra earthquake, *Science*, *337*(6095), 724–726, doi:10.1126/science.1224030.

Ni, S., H. Kanamori, and D. Helmberger (2005), Energy radiation from the Sumatra earthquake, *Nature*, *434*(7033), 582–582.

Okuwaki, R., Y. Yagi, and S. Hirano (2014), Relationship between high-frequency radiation and asperity ruptures, revealed by hybrid back-projection with a non-planar fault model, *Sci. Rep.*, *4*, 7120, doi:10.1038/srep07120.

Parsons, T., R. S. Yeats, Y. Yagi, and A. Hussain (2006), Static stress change from the 8 October, 2005 M = 7.6 Kashmir earthquake, *Geophys. Res. Lett.*, *33*, L06304, doi:10.1029/2005GL025429.

Pathier, E., E. J. Fielding, T. J. Wright, R. Walker, B. E. Parsons, and S. Hensley (2006), Displacement field and slip distribution of the 2005 Kashmir earthquake from SAR imagery, *Geophys. Res. Lett.*, *33*, L20310, doi:10.1029/2006GL027193.

Reif, C., G. Masters, P. Shearer, and G. Laske (2002), Cluster analysis of long-period waveforms: Implications for global tomography, *Eos Trans. AGU*, *83*(47), 954.

Rost, S., and C. Thomas (2002), Array seismology: Methods and applications, *Rev. Geophys.*, *40*(3), 1008, doi:10.1029/2000RG000100.

Singh, D. D., and H. K. Gupta (1980), Source dynamics of two great earthquakes of the Indian subcontinent: The Bihar-Nepal earthquake of January 15, 1934 and the Quetta earthquake of May 30, 1935, *Bull. Seismol. Soc. Am.*, *70*(3), 757–773.

Smith, W. H. F., and D. T. Sandwell (1997), Global sea floor topography from satellite altimetry and ship depth soundings, *Science*, *277*(5334), 1956–1962, doi:10.1126/science.277.5334.1956.

Walker, K. T., M. Ishii, and P. M. Shearer (2005), Rupture details of the 28 March 2005 Sumatra M_w 8.6 earthquake imaged with teleseismic P waves, *Geophys. Res. Lett.*, *32*, L24303, doi:10.1029/2005GL024395.

Wang, D., J. Mori, and T. Uchide (2012), Supershear rupture on multiple faults for the M_w 8.6 Off Northern Sumatra, Indonesia earthquake of April 11, 2012, *Geophys. Res. Lett.*, *39*, L21307, doi:10.1029/2012GL053622.

Xu, Y., K. D. Koper, O. Sufri, L. Zhu, and A. R. Hutko (2009), Rupture imaging of the M_w 7.9 12 May 2008 Wenchuan earthquake from back projection of teleseismic P waves, *Geochem. Geophys. Geosyst.*, *10*, Q04006, doi:10.1029/2008GC002335.

Yagi, Y., A. Nakao, and A. Kasahara (2012), Smooth and rapid slip near the Japan trench during the 2011 Tohoku-Oki earthquake revealed by a hybrid back-projection method, *Earth Planet. Sci. Lett.*, *355–356*, 94–101, doi:10.1016/j.epsl.2012.08.018.

Zhan, Z., H. Kanamori, V. C. Tsai, D. V. Helmberger, and S. Wei (2014), Rupture complexity of the 1994 Bolivia and 2013 Sea of Okhotsk deep earthquakes, *Earth Planet. Sci. Lett.*, *385*, 89–96, doi:10.1016/j.epsl.2013.10.028.